SEISMIC PERFORMANCE OF BRIDGES WITH PIER WALLS

Shi Qi W. Wang, Tracy C. Becker

Department of Civil and Environmental Engineering
University of California, Berkeley

Abstract

Following experimental testing of large scale pier walls, a simple numerical model is implemented to model the interaction effects of biaxial flexure, shear, and sliding. Based on test observations, a phenomenological hysteretic sliding model is suggested to capture flexure induced sliding behavior. Such a model should have both strength and stiffness degradation with increasing sliding displacements and cyclic loading, as well as a method to transfer load back into the flexural mechanism during the rocking phase of sliding motion. A provisional model is implemented in OpenSees using currently available formulations and applied to a model of the experimental walls. The results indicate promising behavior in matching the fundamental period with the measured data, but further refinement is needed to fully capture sliding and behavior at large displacements.

Introduction

In bridges over highways and waterways, short bridge pier walls may be used instead of conventional column piers. These walls are typically squat walls with an aspect ratio less than 1.0 which results in force transfer through shear or flexure-shear action which can be less ductile and less predictable than flexural failure behavior in more slender walls. Unlike building walls, pier walls must resist the lateral loads in both the strong and the weak axis and are often detailed with less vertical reinforcement ratio and with crossties throughout the plastic hinge. Due to the geometry and loading of pier walls, complicated interaction can exist between strong and weak axis flexure and different shear failure mechanisms such as diagonal tension, diagonal compression, and sliding shear. Cyclic degradation is also a factor under seismic loading which may lead to earlier fracture of the vertical reinforcing bars or sliding failure.

Due to the geometry, reinforcement detailing, and loading differences between pier walls and squat walls used in buildings, the conclusions of past literature may not be fully applicable. Thus, an experimental program was done on six large scale pier walls to determine the strength and ductility capacity of these walls under cyclic biaxial loading. A phenomenological model is suggested to capture the sliding mechanism observed during the tests. This modeling technique is then transferred and compared to pier walls in CSMIP monitored bridges.

Experimental testing and results

Six cyclic tests of pier walls were conducted at the Structures Laboratory at UC Berkeley to investigate the strength and displacement capacity of typical pier walls as well as several novel designs. Walls 1-3 were the same design, representative of typical Caltrans detailing. The

three walls were tested under different biaxial loading protocols to study the influence of loading protocol on specimen behavior. Wall 1 was tested uniaxially and Walls 2 and 3 were tested bidirectionally, Wall 2 was tested with a weak-to-strong axis displacement ratio of 4:1 and Wall 3 was tested with a ratio of 8:1. The general geometry of the pier walls is shown in Figure 1. The loading protocol used for the biaxial testing was based on the displacement orbits and the ratio of strong to weak axis displacement of typical pier walls under ground motions.

In general, the specimens exceeded current displacement and ductility predictions and ultimately failed due to the fracture of the vertical reinforcing bars. Significant yielding was observed in the vertical bars which led to the formation of sliding cracks typically near the construction joint of the wall and the footing (see Figure 2). This also led to vertical elongation of the wall, further weaking the sliding plane. In the strong axis, large sliding displacements were present at the later load stages while for the weak axis, a plastic hinge formed near the interface.

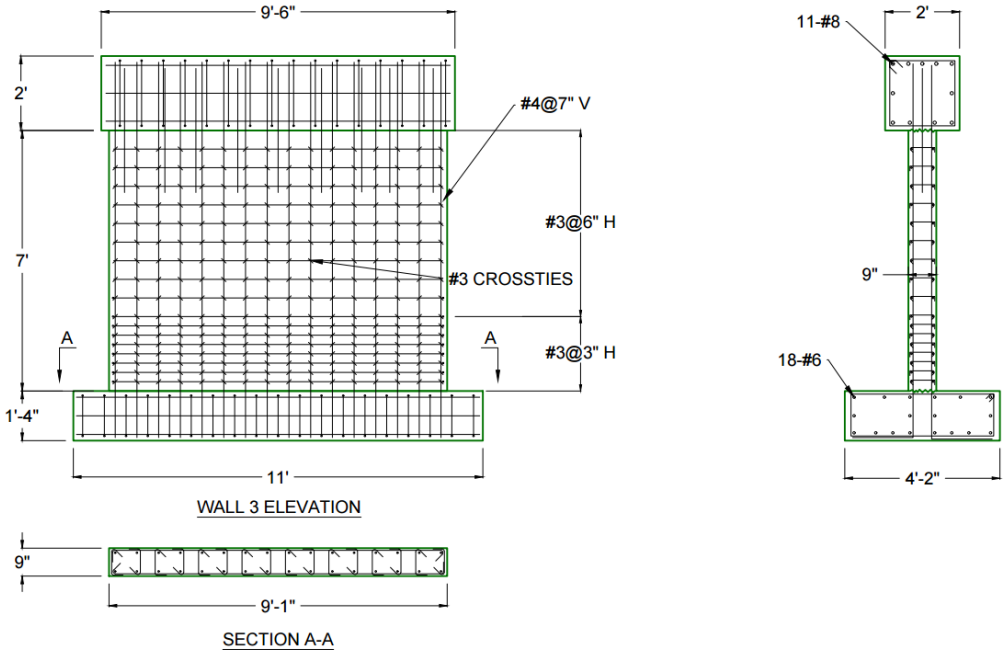

Figure 1. Typical specimen dimensions and detailing for Walls 1-3.

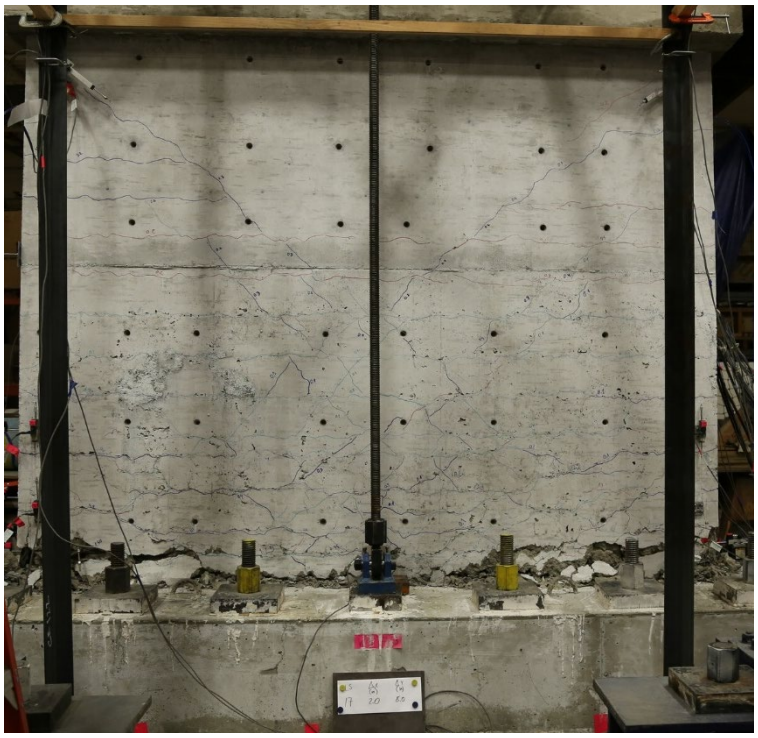

Figure 2. Wall 3 test after the final load stage.

General hysteresis plots of the tests are shown in Figure 3 and 4. The increase in the ratio of weak axis to strong axis displacements between Wall 2 and 3 resulted in a slight decrease in the strong axis strength and a significant decrease in the strong axis displacement capacity. Similarly, the weak axis behavior for Wall 2 did not meet the predicted flexural strength from beam theory, as is suggested by the Caltrans Design Criteria (California Department of Transportation, 2019), possibly due to damage in the strong axis.

The approximate relative contribution of the main displacement mechanisms to the tip displacement is shown in Figure 4. These include the flexural displacement based on plastic hinging at the interface (e.g. uplift and rocking), panel shear mainly based on diagonal cracking in the wall panel, and sliding shear due to sliding at the interface. The values shown are imprecise because at low displacement levels there was a large proportion of measurement noise and at high displacement levels several of the instrumentation sensors began to spall off the specimen. It is important to note that all three mechanisms contribute to the behavior. Also, due to the relatively stable load carrying capacity of the walls near the peak strength, it is inferred that sliding displacements, if controlled and predictable, may be able to augment the displacement capacity of these pier walls in design.

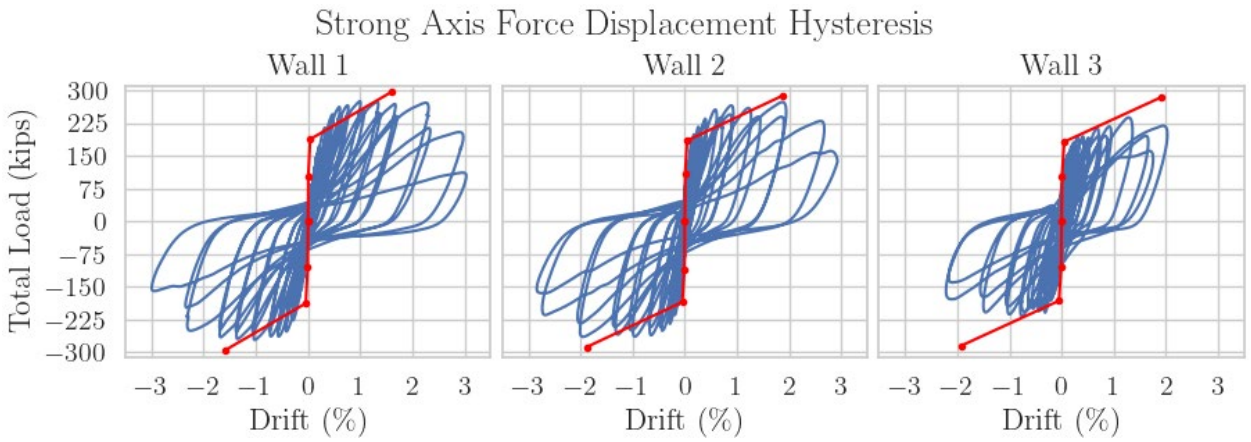

Figure 3. Strong axis hysteresis of tested walls. The points corresponding to flexural cracking, yield, and ultimate are overlaid in red.

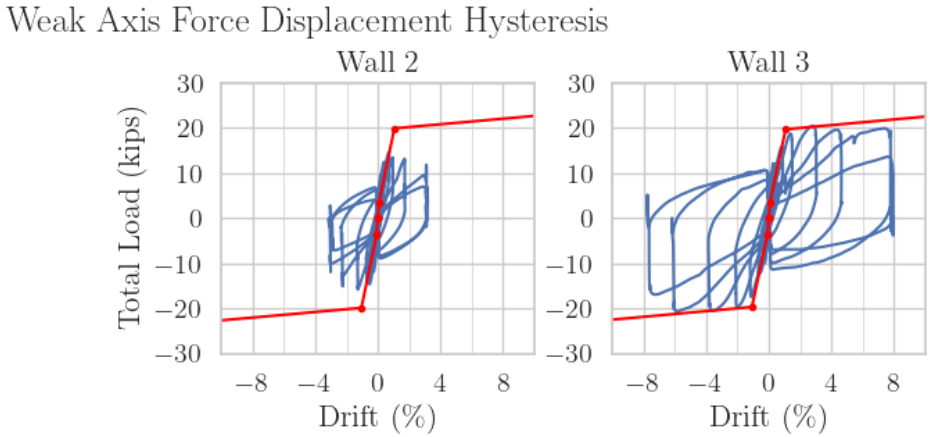

Figure 4. Weak axis hysteresis of tested walls. The points corresponding to flexural cracking, yield, and ultimate are overlaid in red.

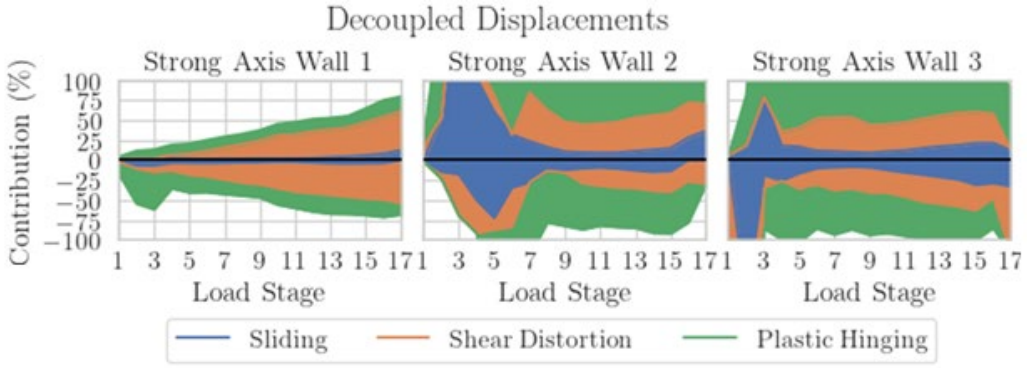

Figure 5. Relative contribution of main displacement mechanisms to tip displacement in the strong axis.

Sliding shear

Significant sliding displacements were observed during the test; however, most shear wall models do not include this deformation behavior. Thus, several sliding shear and interface shear strength prediction equations are compared with the measured peak strengths in the strong axis in Figure 3. These include: the ACI 318-19 provisions (ACI Committee 318, 2019) for interface shear strength, which is based on friction with the vertical bars acting as a clamping force; the ASCE 41-23 guidelines (American Society of Civil Engineers, 2023), which is also based on friction but includes a modification factor for the moment strength of the wall; and the proposed equations by (Vasiliki Palieraki et al., 2022), which separate out the friction and steel dowel contributions.

Despite the additional considerations for cyclic strength in the formulation by Palieraki et al., the measured peak strengths were below the predictions. The measured strengths were also significantly below ACI 318 predictions but were much closer with the ASCE 41-23 predictions. This may be due to the initiation of sliding in the test caused by flexural cracking, which may be better captured by the ASCE41-23 equations that include a term for shear at flexural moment strength. The reduction of sliding resistance due to both cyclic degradation and flexural induced cracking may not be fully accounted for in past literature and design codes. In the case of taller squat walls or squat walls with low reinforcement ratios, the yielding of the longitudinal bars can lead to large sliding crack widths and hence lower sliding resistance.

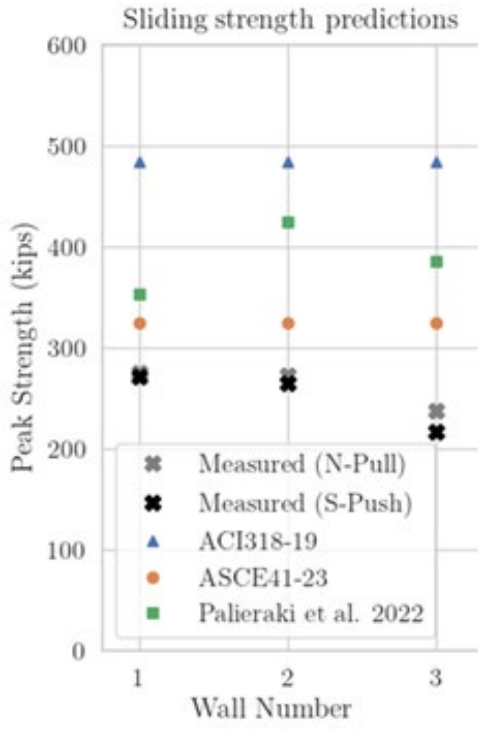

Figure 6. Sliding strength predictions from codes and literature compared to experimental peak strengths.

A Mechanical Sliding Model

A detailed load displacement response for the sliding mechanism in squat walls was proposed by (Trost et al., 2019). In particular, they considered flexural induced cracking and proposed a model to calculate the crack width for a given sliding displacement such that the force resultant from the sliding resistance matches the main diagonal strut angle of the wall. This model is more robust for large sliding displacements and crack widths and considers both sliding resistance from aggregate interlock as well as dowel resistance from kinking of the steel bars. The concrete and steel contributions to the sliding resistance are added together.

Based on the crack width and sliding displacement, the contact areas between two spherical cement grains are integrated over the compression zone to obtain the resultant normal and shear forces. After including the forces in the rebar, based on calculating the rebar elongation assuming a deformed rebar shape, the ratio of the normal to shear stresses is compared the angle of the main diagonal strut. A key assumption is that the shear force is transferred only through the compression zone, since the rebar in the tension zone has already yielded. The crack width is not directly related to the flexural crack width due to elongation of the vertical bars and is simply chosen to satisfy equilibrium. Further, the sliding resisting force is directly proportional to the assumption of the compression zone area. Since the relationship between sliding displacement and flexure is not explicitly known, the exact compression zone area for any sliding displacement cannot be directly calculated.

A numerical implementation is required to calculate the crack widths and sliding resistance for a given sliding displacement. In the case of the pier walls, both the diagonal strut angle and compression zone area is assumed constant and are estimated as the aspect ratio of the wall and the compression zone depth at ultimate flexural strength, respectively.

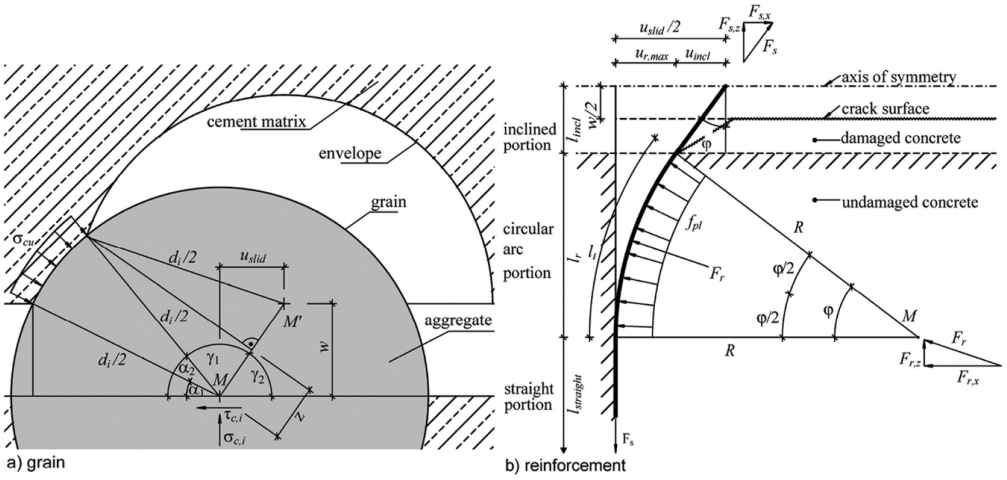

Figure 7. Sliding mechanical model adapted from (Trost et al., 2019)

Modelling of the experimental walls

A numerical model of the pier wall was implemented in OpenSees (McKenna et al., 2010). For squat shear walls, the interaction between shear and flexure becomes more critical

due to the low aspect ratio of the wall. However, full 3D material models and elements require careful calibration of the parameters and significant computation time, as well as careful meshing and constitutive assumptions. Possible approaches to capture shear and flexure interaction include creating a shell model with several layers, each of which use planar concrete and steel materials, as done by (Luu et al., 2017). However, reinforcement is smeared across the layer and failure of individual bars cannot be as easily modelled. Also, further tuning of material parameters may be required to obtain the desired response compared to those in a fiber section.

Another approach is to extend the MLVLEM approach used for slender shear walls to use concrete panel elements for each of the macro fibers instead of uniaxial elements. These elements could have built in shear and flexure interaction, as was done by (Massone et al., 2021). This model was extended to 3D by combining the in-plane wall behavior with an independent and linearly elastic shell element for the out of plane behavior. However, the extension of this model into incorporating weak axis effects is insufficient for pier wall analysis as the nonlinear weak axis behavior is important as is the bidirectional coupling. Importantly, models that were developed for building walls also do not capture the sliding mechanism that was consistently observed at large displacements.

Instead, a phenomenological model is approached for the sliding mechanism. The current implementation uses a hysteretic model based on the ‘Concrete02’ material to capture both strength and stiffness degradation. A stiff compression only spring with a displacement offset is added to represent when the mechanism transfers from sliding to rocking, however currently this implementation is limited to allow for a constant sliding displacement. Ideally the amount of sliding displacement before rocking would slowly increase as the specimen is displaced and cycled.

Sliding spring

As the sliding mechanism is localized to the plastic hinge and mainly concentrated along a single interface crack, it was decided to attach a sliding spring at the base of the cantilever element. This sliding spring should be in series with the flexural spring from the element and any panel shear springs also defined. As seen in Figure 5, there was significant displacement contribution from flexural, panel shear, and sliding deformations, which affirms the choice to place these springs in series. This sliding spring is only present in the strong direction due to limited sliding displacement observed in the weak direction.

An ideal phenomenological model of the sliding spring is proposed following test observations. Sliding did not begin until significant horizontal cracking, indicating that the initial stiffness of the sliding spring should be large, possibly larger than the panel shear stiffness. Sliding occurred and increased gradually as the wall was damaged, resulting in a lower sliding resistance as the interface crack widened. The plastic elongation of the vertical bars due to cyclic loading and ratcheting effects further widened the interface crack. Thus, the sliding spring should have strength degradation as the sliding displacement is increased, as well as due to cyclic loading.

It is conceivable that there is a maximum sliding resistance dependent on the wall geometry, reinforcement and concrete properties, and the axial load. This also requires that the

sliding spring be in series with the flexural spring due to the large initial sliding stiffness. Since sliding, flexural, and shear displacements remained significant throughout the test, the relative stiffnesses of these springs in series should remain fairly constant. However, the flexural stiffness of the wall reduces as concrete spalls and the specimen becomes damaged. This then requires that the sliding spring experience a similar stiffness degradation in order to keep the relative stiffnesses constant. Thus, softening of the sliding spring on subsequent cycles is required, which can be approximated by the 'Conrete01' and 'Concrete02' materials in OpenSees. During unloading, the sliding resistance should reduce quickly as the compression surfaces are pulled apart and aggregate interlock resistance reduces.

During the later stages of the test, it was observed that the wall would slide and rock once the buckled and kinked vertical bars were stretched and re-engaged (Figure 8). During the sliding phase, there was no significant change in the strength until the rocking phase started, at which point the load would increase due to strain hardening of the vertical bars under flexure. This indicates that once sliding occurs, the sliding stiffness decreases significantly but eventually needs to increase again during this rocking phase. One option could be to model this with a large 'bearing' stiffness on the sliding spring to encourage the flexural section to take up the displacement at large lateral displacements.

Figure 8. Sliding interface of Wall 3 after the test. The vertical bars are kinked.

The amount of sliding displacement that occurs before the rocking phase is a function of the level of kinking on the vertical bars. Just after the onset of sliding, the interface crack and level of spalling is small so the vertical bars are deformed plastically only over a short length. This means only a small sliding displacement is required before rocking occurs. In contrast, at later stages of loading where there is a large interface crack and when the kinking deformation of the vertical bars is over multiple inches, a larger sliding deformation is required before rocking occurs. In our sliding spring model, this could mean constantly adjusting the displacement at which bearing occurs. For instance, perhaps every load cycle that reaches the sliding load-displacement backbone is allowed to slide a small increment before a large bearing stiffness takes over to re-engage the flexural mechanism. This would mean that the amount of sliding

deformation depends on the number of times the specimen has been cycled beyond the current sliding strength, instead of remaining constant (as in bearing).

Currently, there is no well documented material implanted in OpenSees that has all of these characteristics. Without developing a custom uniaxial element, it is possible to approximate most of these characteristics, except changing the sliding displacement before bearing. To do so, a 'Concrete02' material is placed in parallel with a bearing spring, which is composed of an elastic compression only material ('ENT') that is offset with some initial displacement. The 'Concrete02' material parameters for peak strength, initial stiffness, and post peak stiffness are based on the sliding load-displacement backbone curve from the (Trost et al., 2019) model. The 'lambda' parameter should be set to a small number, around 0.02, to encourage more stiffness degradation back to the origin. The tensile strength and stiffness of the 'Concrete02' is set to small values as they are not needed, but 'Concrete02' is chosen instead of 'Concrete01' because of the initial elastic unloading portion. The currently chosen sliding spring hysteresis is shown in Figure 9.

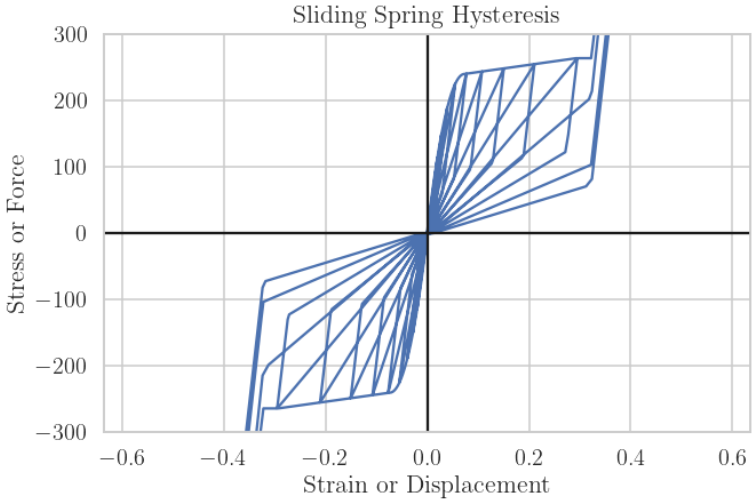

Figure 9. Currently implemented sliding spring hysteresis based on the 'Concrete02' material.

Biaxial interaction and element choice

As demonstrated by our experiments, there is a non negligible interaction between large deformations in the strong and weak axis. Large inelastic strains due to flexure in both directions can cause earlier fracture in the vertical bars due to biaxial stresses forces or low cycle fatigue. Depending on the ratio of current and previous cycle weak to strong axis displacements, the strong axis or weak axis strength and displacement capacity may be reduced. In terms of modelling, this means that an accurate pier wall model cannot have the strong and weak axis independent from each other, as is the case with the MVLEM series of models.

The conventional fiber model typically used for beam analysis is able to couple the bidirectional flexure and axial response; however it does not account for shear interaction nor shear deformation. To account for shear deformation, a shear spring is added in series based on a bilinear curve proposed by (Sozen & Moehle, 1993).

One method of including shear and flexure interaction could be to use multidimensional material models for the fibers rather than the typical uniaxial materials used in beam analysis. In OpenSees this could be accomplished with “NDFiber” sections and “NDMaterial” materials. However, due to the complexity of defining the hysteretic behavior of 3D materials, there are relatively few robust, well tested, and well documented nonlinear materials currently implemented in OpenSees.

Another possible method of creating some interaction is to use the fiber section to provide the flexural and axial stiffness of a link member (‘twoNodeLinkSection’ in OpenSees). In this element, shear springs for panel shear (and possibly sliding) can also be defined and will interact with the flexural springs through the geometry of the link. Although not strictly a material model interaction, the shear spring stiffnesses will affect the rotational degree of freedom at the element ends. This approach was attempted, however a software bug in the current version of OpenSees led to inconsistent results. As a result, the current model uses a simplified beam fiber model with springs at the base to represent the panel shear and sliding shear effects. The fiber model allows a relatively accurate definition of the wall geometry and reinforcement, as well as allowing use of conventional uniaxial material models for steel and concrete.

Material models

The material models used for the fiber section are ‘Concrete02’ and ‘Steel02’ for the confined concrete, cover concrete, and rebar materials. Effective confinement factors are calculated based on the reinforcement layout and typical values for the other parameters are taken from design codes or previous literature. A fracture and buckling strain for the steel material is defined as 0.20 and the residual strain of the core concrete and implemented with a ‘MinMax’ material wrapper. As suggested by (Marafi et al., 2019), the concrete materials are regularized based on a constant fracture energy in compression to provide mesh objective results when using the displacement element formulation.

Experimental comparison

For the wall analysis, the gravity load is first applied to the model at the top node and held constant. Then, the displacement as measured by the actuators from the Wall 3 test is applied (Figure 10). Three different models are compared to the experimental results, the first of which only uses a fiber model with a fixed base, the second with the bilinear panel shear spring added in both directions, and the third with the sliding spring added in series only in the strong direction (Figure 11). When the resulting hysteresis is compared with the experimental results for Wall 3, several discrepancies are seen. The fiber only model greatly overpredicts the peak strong axis force while the fiber plus shear spring model matches the general shape the experimental hysteresis but with larger forces. More pinching was also observed experimentally.

In the full model with the sliding spring and the shear panel spring, there are almost no global hardening effects in the test results while the model shows significant hardening post yielding in the strong axis. This may be due to the implementation of the panel shear spring as no failure point is defined. As the flexural spring softens, more load will be taken by the panel shear spring due to the constant stiffness of the post-cracking portion. The re-loading slopes in the

experiment also soften faster than what was captured in the model. There is also an imprint of the sliding spring in the initial stage, leading to a sharp peak right around yielding. This still persists even if the negative slope portion of the sliding spring is replaced with a zero-slope region. Because the current implementation of the sliding spring always has bearing occur at the same displacement (currently at around 0.35 inches for the experimental wall model), the flexural behavior will only begin after that drift ratio (around 0.4%).

In the weak axis, the fiber only model provides a good estimation of the ultimate strength but overpredicts the peak strength, possibly due to not capturing cracking or spalling effects due to dilation of the vertical bars under compression. Also, the model greatly overpredicts the peak flexural strength once the panel shear spring is added. Since plastic hinging was observed in the weak axis at large displacements, adding in the shear spring in series in the weak direction may not be appropriate.

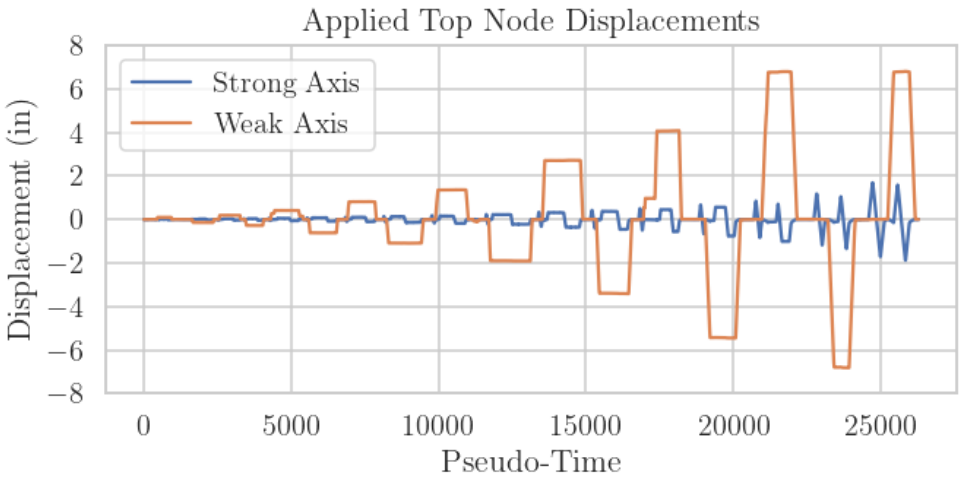

Figure 10. Applied displacement history to the top node

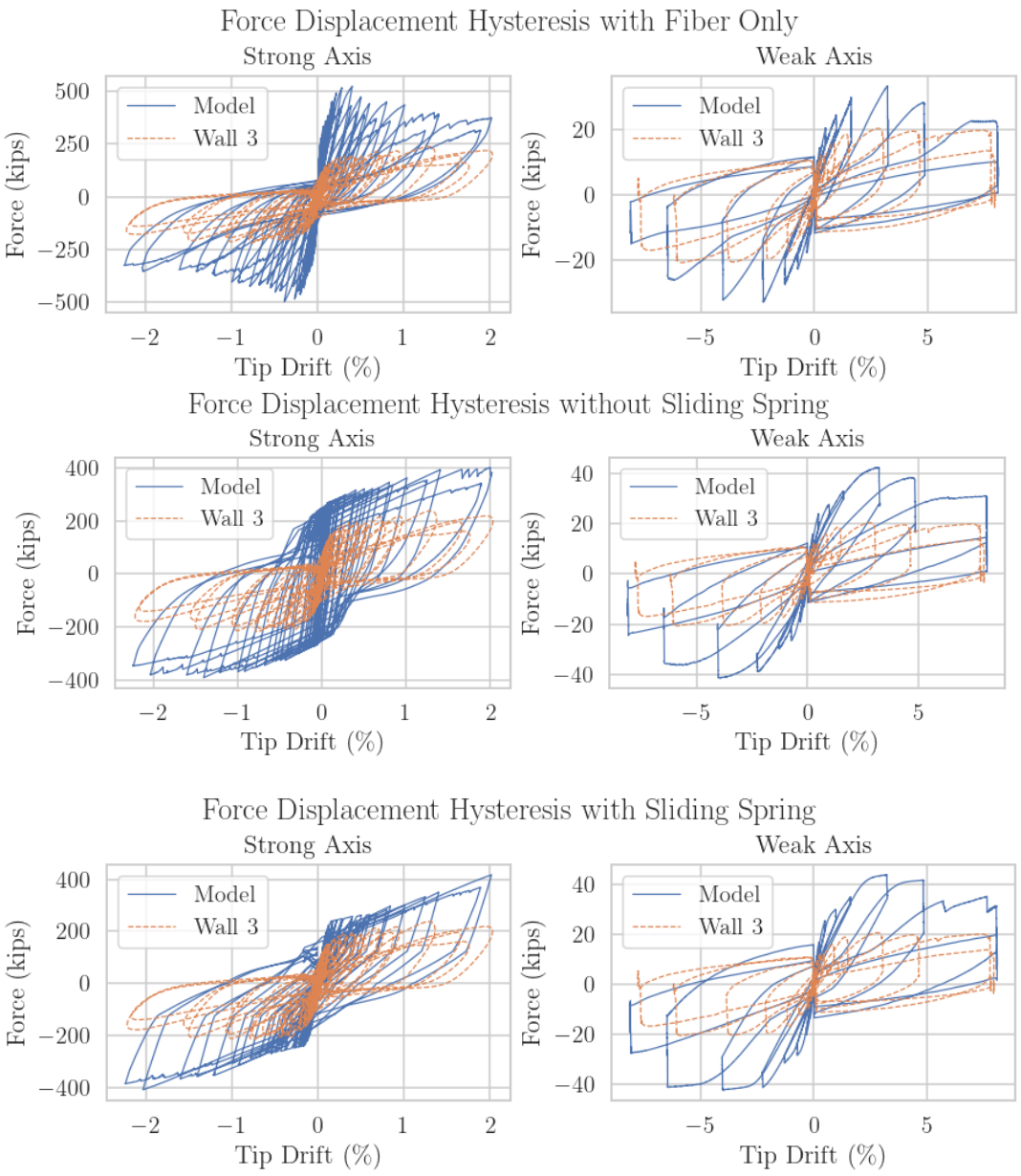

Figure 11. Comparison of numerical model and experimental results for Wall 3 for three different numerical models.

CSMIP pier wall models

Similar pier wall models were created for both the Klamath River Bridge ('Klamath') and the Hwy 101/156 overpass bridge ('156') CSMIP instrumented pier wall bridges. The geometry and reinforcement details were adapted into a fiber section model based on the construction drawings. Typical grade 60 steel and 4 ksi strength concrete was assumed. The mass of the superstructure above each pier was assumed based on the bridge girder size and typical concrete

and steel density. A 2 inch thick asphalt topping was also assumed for mass and gravity load. Five percent modal damping in the first mode was assumed.

For the 156 bridge, the infill reinforced concrete wall is assumed to be fully connected to the previous concrete columns. Effective confinement values are calculated for the infill wall portion and the columns. As the superstructure consists of 5 steel girders and a thin deck, the overall tributary weight per bent was calculated to be about 270 kips. The fiber section can be seen in Figure 12. An average pier height of 14 feet was used for the model.

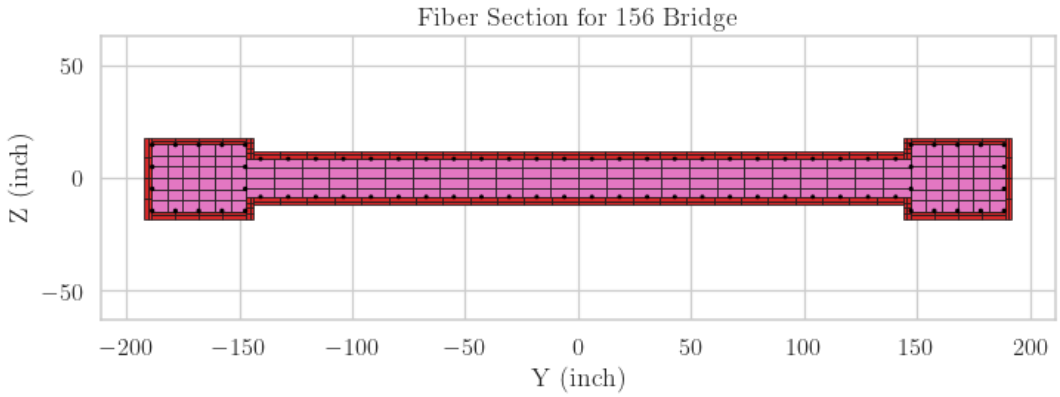

Figure 12. Fiber section used for the 156 bridge.

Contrastingly, the Klamath bridge consists of multiple hollow concrete piers that support a large span of around 180 feet. A concrete box girder is used for the superstructure which leads to a large estimated tributary weight of 2000 kips per pier. Interestingly, the vertical longitudinal bars are placed on the outside of the horizontal stirrups and so accordingly the entire section was taken as unconfined concrete. An average pier height of 50 feet was used and the curved portions of the cross section was approximated by the fiber model in Figure 13. Due to the larger aspect ratio (on average about 1.67), no sliding spring was added for the Klamath bridge model as the more slender flexural portion would contribute more to the displacements.

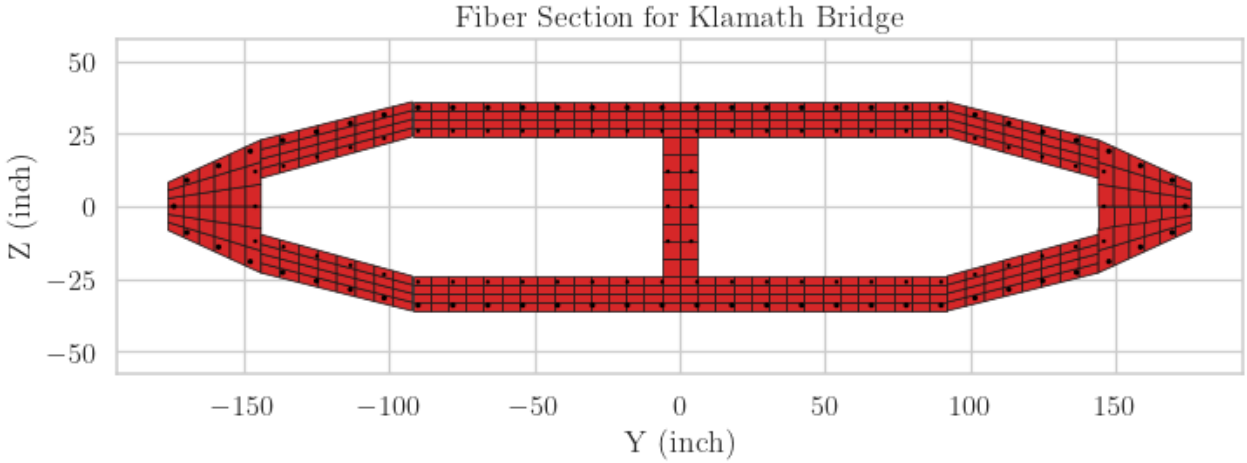

Figure 13. Fiber section used for the Klamath bridge.

Model results

To investigate the nonlinear behavior of the model, the same displacement protocol for the wall test was applied to the 156 and Klamath pier wall models, after scaling by the height as to apply the same drift ratios. In the results presented in Figure 15, the sharp reduction in strength post peak for the Klamath bridge is seen due to the lack of confinement in the pier wall. Both walls have a reduction in weak axis strength post peak while the 156 wall is predicted to be more ductile due in part to the sliding mechanism. From eigenvalue analysis, the first mode natural period for the 156 and Klamath bridge are 0.13 seconds and 0.81 seconds respectively.

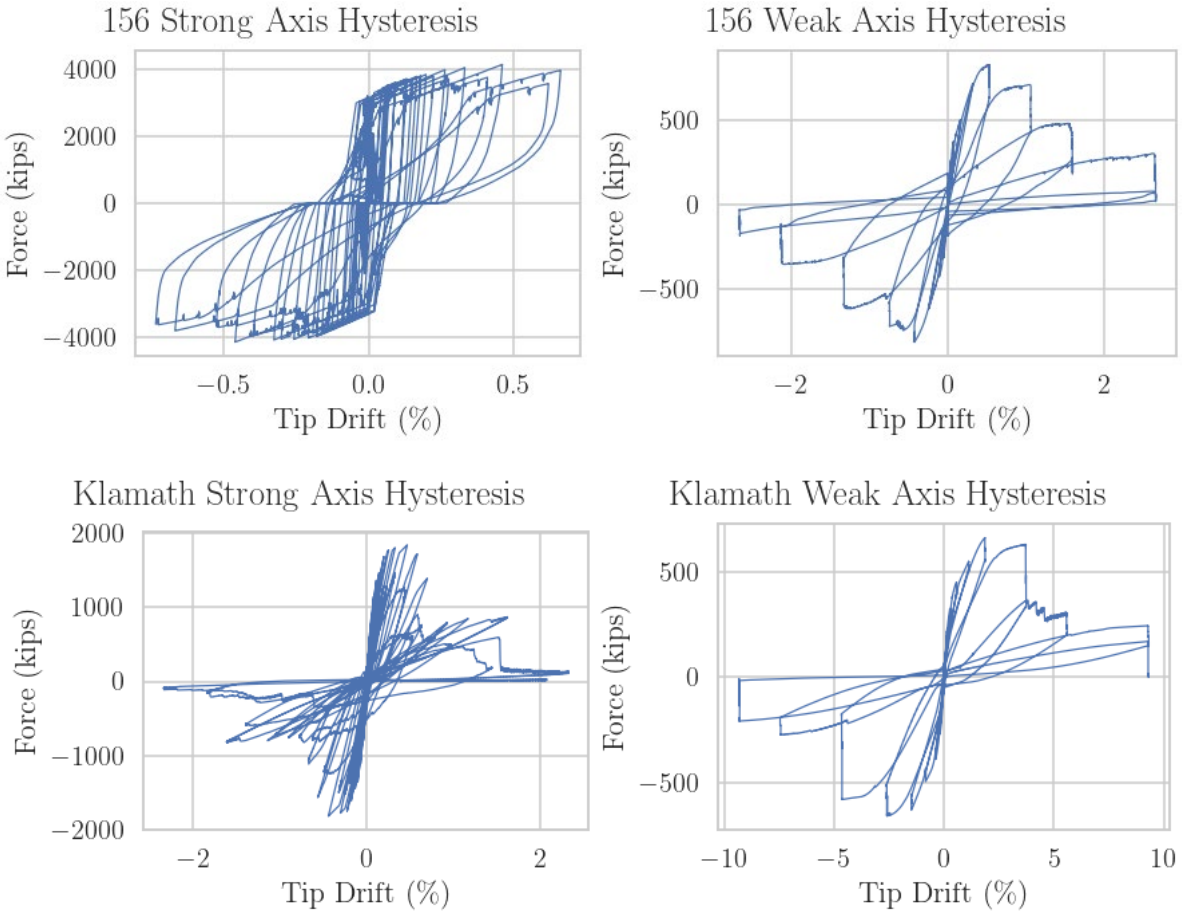

Figure 14. Hysteresis graphs of the models for the 156 and Klamath bridge.

To compare with the measured ground motions, for the 156 bridge, seven ground motion records are available. The acceleration time history of the measured response at the top of one of the piers is input into a Fourier transform to obtain the measured natural period, as shown in Figure 15. The sensor data was already aligned with the pier strong and weak directions. From the graph, an approximation for the periods is about 0.2 seconds in the weak direction and 0.11 seconds in the strong direction. It is noted that several of the motions have small accelerations so there may be significant measurement noise. The fundamental period of the 156 bridge is similar to the numerical model period of 0.13 seconds.

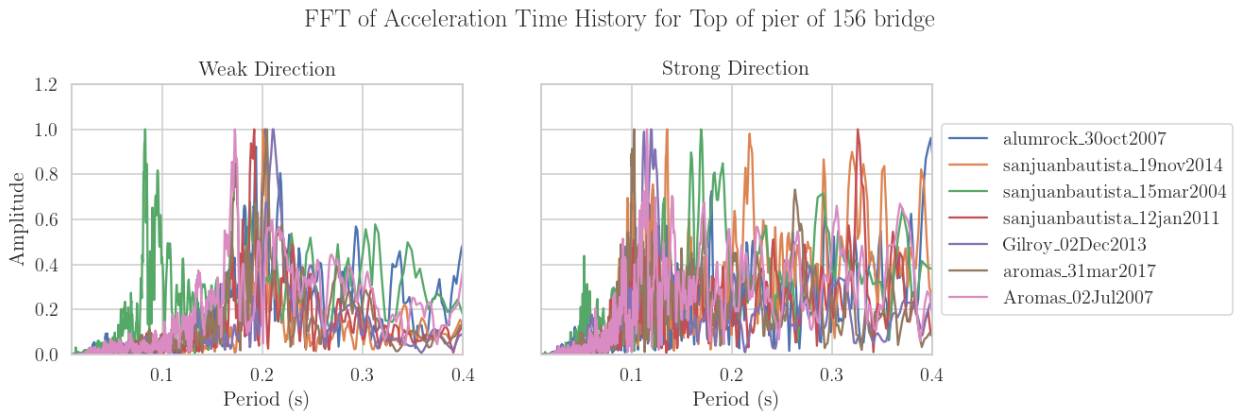

Figure 15. Measured frequencies of the 156 bridge.

For the Klamath bridge, only two ground motions are recorded. The 'crescentcity' ground motion is selected as it has the largest PGA of around 0.02g. This record shows natural periods of 0.54 seconds and 0.55 seconds for the weak and strong axis, as seen in Figure 16. The lack of period separation in the weak and strong axis as measured by the sensors may be due to the increased effective stiffness in the pier weak axis (bridge longitudinal) due to the long bridge span tying together multiple piers in the weak axis. The natural period measured is also lower than our model natural period of 0.81 seconds, suggesting that a simple cantilever model may not be sufficient when modelling this bridge.

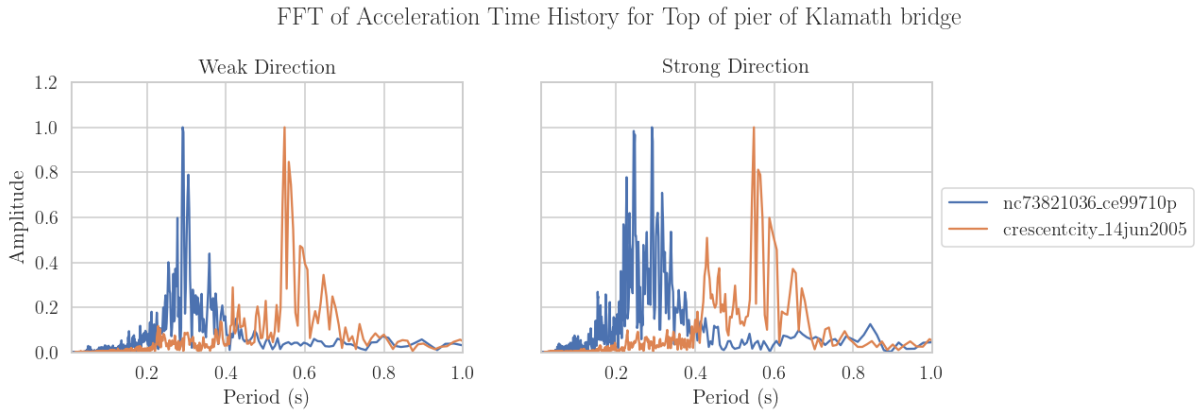

Figure 16. Measured frequencies of the Klamath bridge.

Caveats

When comparing the results from the numerical models to the recorded data, several limitations should be kept in mind. First, the recorded motions for these pier wall bridges have a low maximum acceleration, which limits the validation to the elastic regime. Second, only two motions were available for the Klamath bridge and only the 156 bridge has a free field sensor which is most apt to apply as a uniform excitation. The recorded motions also consider the combined effect of the abutments and the entire bridge deck, which can tie together several adjacent pier walls. In the model, we are currently only looking at the natural frequency of a single pier wall. The natural frequency of the model is also heavily dependent on the estimation

of the tributary mass, and to a lesser extent, the stiffness of the material and geometry of the fiber section. As these values were estimated from the construction drawings, high precision of the results cannot be guaranteed.

A more complete pier wall model would also consider the flexibility of the wall foundation as the flexibility of the footing can greatly affect the overall stiffness and displacement capacity of the pier. The large in plane stiffness of the pier wall compared to the footing rotation stiffness can cause large footing rotations, which depend on soil structure interaction. Lastly, the currently implemented sliding shear model does not yet directly consider how the plastic elongation of the vertical rebar near the interface crack affects the width of the crack. The effect of crack width on the strength and stiffness degradation of the sliding mechanism requires more exploration to properly quantify.

Future plans

To capture the increase in allowable sliding deformations after cyclic degradation, a new hysteretic sliding behavior needs to be defined and implemented in OpenSees. Further investigation of the previously alternative element formulations (‘NDFiber’, ‘twoNodeLinkSection’) will be carried out. Next, a global bridge model will be developed to consider the effect of multiple pier walls tied together with the bridge superstructure. Abutment springs would be added based on the guidelines set out by (California Department of Transportation, 2019) and the displacement history response of the CSMIP instrumented pier wall bridges will be compared against those of the model.

References

ACI Committee 318. (2019). *ACI318-19 Building Code Requirements for Structural Concrete and Commentary*. https://doi.org/10.14359/51716937

American Society of Civil Engineers. (2023). *Seismic Evaluation and Retrofit of Existing Buildings: ASCE/SEI 41-23*. American Society of Civil Engineers. https://doi.org/10.1061/9780784416112

California Department of Transportation. (2019, April). *Caltrans Seismic Design Criteria Version 2.0*.

Luu, C. H., Mo, Y. L., & Hsu, T. T. C. (2017). Development of CSMM-based shell element for reinforced concrete structures. *Engineering Structures*, *132*, 778–790. https://doi.org/10.1016/j.engstruct.2016.11.064

Marafi, N. A., Ahmed, K. A., Lehman, D. E., & Lowes, L. N. (2019). Variability in Seismic Collapse Probabilities of Solid- and Coupled-Wall Buildings. *Journal of Structural Engineering*, *145*(6), 04019047. https://doi.org/10.1061/(ASCE)ST.1943-541X.0002311

Massone, L. M., López, C. N., & Kolozvari, K. (2021). Formulation of an efficient shear-flexure interaction model for planar reinforced concrete walls. *Engineering Structures*, *243*, 112680. https://doi.org/10.1016/j.engstruct.2021.112680

McKenna, F., Scott, M. H., & Fenves, G. L. (2010). Nonlinear Finite-Element Analysis Software Architecture Using Object Composition. *Journal of Computing in Civil Engineering*, *24*(1), 95–107. https://doi.org/10.1061/(asce)cp.1943-5487.0000002

Sozen, M. A., & Moehle, J. P. (1993). *Stiffness of reinforced concrete walls resisting in-plane shear* (EPRI Research Project Nos. 3094–1).

Trost, B., Schuler, H., & Stojadinović, B. (2019). Sliding in Compression Zones of Reinforced Concrete Shear Walls: Behavior and Modeling. *ACI Structural Journal*, *116*(5). https://doi.org/10.14359/51716755

Vasiliki Palieraki, Elizabeth Vintzileou, & John F. Silva. (2022). Interface Shear Strength under Monotonic and Cyclic Loading. *ACI Structural Journal*, *119*(3). https://doi.org/10.14359/51734519